Directing Noble Metal Ion Chemistry within a Designed Ferritin Protein[†,‡]

Christopher A. Butts, Joe Swift, Seung-gu Kang, Luigi Di Costanzo, David W. Christianson, Jeffery G. Saven, and Ivan J. Dmochowski*

Department of Chemistry, University of Pennsylvania, 231 South 34th Street, Philadelphia, Pennsylvania 19104-6323

Received September 3, 2008; Revised Manuscript Received October 12, 2008

ABSTRACT: Human H ferritin (HuHF) assembles from 24 four-helix bundles to form an ~500 kDa protein with an 8 nm internal cavity. HuHF provides a useful model for studying the transport of metal ions in solution to buried reaction sites in proteins. In this study, HuHF was redesigned to facilitate noble metal ion (Au^{3+}, Ag^{+}) binding, reduction, and nanoparticle formation within the cavity. Computationally determined amino acid substitutions were targeted at four external and four internal surface sites. A variant with a total of 96 cysteines and histidines removed from the exterior surface and 96 non-native cysteines added to the interior surface retained wild-type stability and structure, as confirmed by X-ray crystallography, and promoted the formation of silver or gold nanoparticles within the protein cavity. Crystallographic studies with HuHF variants provide insight into how ferritins control access of metal ions to interior residues that perform chemistry.

Polypeptides play important roles in the biological synthesis of many minerals (e.g., silicates (*1*), carbonates (*2*), and phosphates (*3*)) and biologically derived particles of copper (*4*), iron (*5*), silver (*6, 7*), and gold (*8*). The molecular details of such syntheses, however, are not always well understood. Polypeptide-mediated biomineralization typically occurs under ambient temperatures and pressures and leads to structures (e.g., magnetic iron oxide particles and corals) that are ordered on both nano- and macroscale dimensions. Despite long-standing interest in biomineralization processes, few systems involving such nanoparticles and their peptides and metal ions have been structurally characterized in molecular detail (*1, 9*). For this reason, we have embarked on a program to investigate and reengineer ferritin proteins. We demonstrate in this work that sequence and structural changes to human H ferritin (HuHF),[1] which were guided by computation and verified by X-ray crystallography, can yield a protein with new abilities to form gold and silver nanoparticles within its interior.

Noble metal nanoparticles have useful optical and electronic properties, as well as promising applications for biomedicine (*10*−*12*), catalysis (*13, 14*), sensing (*15*), and nanoelectronics (*16*). While water-soluble silver and gold colloids have been described elsewhere using organic passivating agents (*17*−*19*), protein-based assemblies are biocompatible and provide well-defined structures that can be modified site-specifically. HuHF is composed of 24 four-helix bundles that self-assemble to form a hollow spherical protein assembly, M_w ~500 kDa, with roughly 8 nm inner and 12 nm outer diameters. Thus, ferritin provides a vehicle for directing the synthesis of inorganic materials within a preorganized protein framework.

Previously, horse spleen apoferritin (HSAF) was employed in the synthesis of metallic silver (*20, 21*), gold (*22*), palladium (*23*), copper (*24*), cobalt (*25*), and nickel (*26*) nanoparticles. In reactions of HSAF with Ag^{+}, Pd^{2+}, Cu^{2+}, Co^{2+}, or Ni^{2+} and a reducing agent, small particles were formed, indicating incomplete loading of the ferritin cavity. Some ions, such as Fe^{2+}, gain entry to the interior cavity of ferritin through narrow, protein-spanning channels, whereas other metals are believed to interact preferentially with residues on the protein exterior and are largely excluded from the cavity (*27*). Limited evidence exists for mono- or trivalent metals diffusing through the 3-fold channel (*26, 28, 29*). In one example, the presence of Au^{+} and sulfide yielded an Au_2S core within HSAF (*29*). Other examples involved reduction of Au^{3+} or Ag^{+} in the presence of HSAF, which produced particles that exceeded 8 nm in diameter (*20, 22*). These particles were clearly identified on the outer protein surface by TEM, with no evidence of metal deposition inside the cavity.

Dominguez-Vera et al. reported similar results in the synthesis of Ag^0 particles with HSAF using $NaBH_4$ as the reducing agent (*21*). UV−vis measurements showed that the silver surface plasmon resonance (SPR) absorbance band was red shifted by more than 20 nm from typical silver nanoparticles in solution, which may result from particle aggregation. Similarly, TEM images of the unstained Ag-HSAF

[†] Funding was provided by the NIH (GM49758 to D.W.C., GM61267 to J.G.S.) and NSF (DMR-0520020 to J.G.S. and I.J.D., CHE-0548188 to I.J.D.).

[‡] The atomic coordinates of **H8**, Hg^{2+}-**H8**, and Au^{3+}-**H9x** have been deposited in the Protein Data Bank (www.rcsb.org) with accession codes 2Z6M, 3ERZ, and 3ES3, respectively.

* Corresponding author. Phone: (215) 898-6459. Fax: (215) 898-2037. E-mail: ivandmo@sas.upenn.edu.

[1] Abbreviations: BSA, bovine serum albumin; CD, circular dichroism; DLS, dynamic light scattering; FPLC, fast protein liquid chromatography; GuHCl, guanidine hydrochloride; HSAF, horse spleen apoferritin; HuHF, human H-ferritin; ICP-OES, inductively coupled plasma optical emission spectroscopy; IPTG, isopropyl β-D-galactopyranoside; MPD, 2-methyl-2,4-pentanediol; MOPS, 3-(*N*-morpholino)propanesulfonic acid; PDB, Protein Data Bank; RFZ, rotation function *Z* score; SASA, solvent-accessible surface areas; SCADS, statistical computationally assisted design strategy; SPR, surface plasmon resonance; TEM, transmission electron microscopy; TFZ, translation function *Z* score; T_m, melting temperature; **wtH**, wild-type human H-ferritin.

10.1021/bi8016735 CCC: $40.75
Published on Web 11/08/2008

samples indicated close association of the 4 nm silver particles. These results suggest that metal nanoparticle synthesis occurs readily on the more accessible ferritin exterior surface.

The sequence and structures of wild-type proteins can be manipulated so as to control nanoparticle formation. One effort to bias the formation of nanoparticles within the interior of ferritin focused on developing a protein chimera (*30*). An exogenous polypeptide capable of reducing silver was appended to human L ferritin and displayed in the interior cavity, which promoted production of small silver particles. Such exogenous peptides are often unstructured, however, and may occlude interior volume in an uncontrolled manner. An alternate and potentially less disruptive approach is to redesign the sequence of a known ferritin, especially because these proteins can be robust with respect to a wide variety of mutations (*31*). In order to identify nonnatural ferritin nanoreactors with metal binding properties that are tuned to achieve new functions, we have employed computational design for the judicious choice of protein mutations.

Computational redesign of existing proteins allows the simultaneous variation of many residues and has previously yielded structures with novel properties (*32, 33*). Applications include the creation of maquettes (*34*) that bind porphyrins (*35, 36*) or metals (*37*) and proteins with catalytic activity (*38*). Many sequence search methods use pruning and dead-end elimination (*39*), Monte Carlo (*40*), and simulated annealing (*33, 41*) methods. Complementary to these approaches are probabilistic approaches to protein design (*42, 43*), which yield the site-specific probabilities of the amino acids among sequences likely to fold to a given three-dimensional structure (*41, 44*). With their capabilities for considering large numbers of simultaneous interresidue interactions and multiple substitutions, such computational methods are useful for identifying appropriate positions and mutations when engineering proteins. Based on their stability and high symmetry, ferritins are particularly amenable to redesign, as exemplified by a Dps protein that we engineered to contain a cavity with 86% apolar surface area (*31*). Using a similar approach, we have now modified up to 192 residues on the interior and exterior surfaces of HuHF, in order to control noble metal binding, reduction, particle nucleation, and growth within the protein template.

We hypothesized that removal of reactive cysteine and histidine residues on the exterior surface and introduction of additional soft cysteine ligands on the interior surface would promote the formation of gold and silver particles within the cavity. Precedent for this approach appears in work involving other protein assemblies. Within cowpea chlorotic mottle virus, changing native interior basic residues to acidic glutamates promoted the formation of an iron oxide core (*45*). Cysteine residues introduced into the interior of cow pea mosaic virus yielded a protein that maintained its structure and stability (*46*). Similarly, the addition of cysteine residues on the exterior of viral proteins proved to be useful for synthesizing gold clusters (*47*) and binding pre-formed particles (*9*). While these systems highlight the potential benefits of incorporating one or two external cysteine residues on the binding of premade gold particles or gold clusters, they were not designed for incorporation and nucleation of size-constrained noble metal particles. In the present study, the manipulation of histidine and sulfur ligands on both the HuHF exterior and interior surfaces was shown to improve solubility and have minimal effects on structure and stability, while creating a versatile biotemplate for the synthesis of metallic silver or gold nanoparticles. HuHF provides a useful model for studying how proteins are able to control the access of solution metal ions to residues at buried sites that perform chemistry.

MATERIALS AND METHODS

Reagents. Bactotryptone and yeast extract were purchased from Difco. IPTG was purchased from Fisher Biotech. Ampicillin sodium salt was purchased from Fisher Bioreagents. Molecular biology grade GuHCl was purchased from Promega. MOPS was purchased from Sigma. Gold(III) chloride was purchased from Acros Organics. 2,2′-Dipyridyl was purchased from Aldrich. All other chemicals were purchased from Fisher Scientific and were of ACS grade or higher, unless otherwise specified.

Computational Determination of Mutations. On the exterior HuHF surface, all four solvent-exposed cysteines and histidines, C90, C102, H13, and H105, were selected for mutation, in order to generate mutant **H4**. A second mutant was generated, **H8**, which included the four exterior mutations of **H4** and four non-native cysteines on the interior surface.

The X-ray crystal structure used in the computational modeling was human H ferritin (PDB code 2FHA) with Gln-86 substituted for the wild-type Lys (*48*). Sites on the interior surface helices (B and D) were selected based on their SASA, as calculated with the software NACCESS using a probe radius of 1.4 Å (*49*). Residues with more than 50% solvent-accessible area were considered as possible mutation sites. Residues having favorable intra- or intersubunit interactions were discarded from the preliminary set: K49 and K53 were close to the 4-fold axis; K71 and K157 interacted with neighboring residues via interchain salt bridges, whereas N139 made favorable hydrogen bonds. H57 and H60 on the B-helix were also maintained as wild type, in order to maximize metal coordination within the cavity. The remaining five interior surface sites (E64, T135, E140, K143, and E147) were considered for possible substitution with cysteine.

SCADS was employed to estimate the amino acid probabilities at each site considered for mutation (*37, 42*). To facilitate the calculation, a symmetry approximation was implemented, given the 24 identical subunits of HuHF, by imposing that every chain have the same sequence with equivalent residues having identical rotamer states (*31, 44*). Interatomic nonbonding energies were determined using the AMBER potential with a distance-dependent dielectric constant and a modified hydrogen-bonding term with an interatomic cutoff of 8 Å (*42*). No constraints involving solvation preferences (*42*) or secondary structure propensities were imposed. For the exterior surface design, all amino acids were allowed at sites 90 and 102 and all amino acids but Cys were considered at sites 13 and 105. For each of the five interior sites selected for mutation, only Cys and wild-type residues were allowed in each position.

wtH, **H4**, **H8**, *and* **H9x** *Gene Construction.* The **wtH** gene was generously provided by Dr. Paolo Arosio and cloned into a pET-17b vector (Novagen) via PCR by cloning in *Nde*I and *Hin*dIII restriction sites (at 5′ and 3′ ends, respectively). The PCR product was cleaned with the QIAquick PCR

purification kit (Qiagen), doubly digested with *Nde*I and *Hin*dIII restriction enzymes (New England Biolabs) at 37 °C for 1.5 h, and purified on a 1.2% agarose gel by the QIAquick gel extraction kit (Qiagen). The gene was ligated to *Nde*I/*Hin*dIII doubly digested pET-17b vector using the T4 DNA rapid ligation kit (Roche). The **wtH** cDNA served as the template for the **H4** mutant. The following mutations were made in a stepwise fashion using the QuickChange site-directed mutagenesis kit (Stratagene): H13D, C90R, C102A, and H105Q. Primers used for mutagenesis of **wtH** to generate the **H4** mutant are as follows: H13D (forward) 5′, GTGCGCCAGAACTACGACCAGGACTCAGAG; H13D (reverse) 5′, CTCTGAGTCCTGGTCGTAGTTCTGGCGCAC; C90R (forward) 5′, CAAGAAACCAGACCGTGATGACTGGGAGAGCG; C90R (reverse) 5′, CGCTCTCCCAGTCATCACGGTCTGGTTTCTTG; C102A (forward) 5′, GCGGGCTGAATGCAATGGAGGCTGCATTACATTTGG; C102A (reverse) 5′, CCAAATGTAATGCAGCCTCCATTGCATTCAGCCCGC; H105Q (forward) 5′, GGCTGAATGCAATGGAGGCTGCATTACAGTTGGAAAAAAATG; H105Q (reverse) 5′, CATTTTTTTCCAACTGTAATGCAGCCTCCATTGCATTCAGCC. The H105Q primers accounted for the C102A mutation that was made prior to this round of mutagenesis.

The **H8** mutant cDNA was obtained directly from DNA 2.0 (Menlo Park, CA) and doubly digested with *Nde*I and *Hin*dIII restriction enzymes (37 °C, 1.5 h). A 1.2% agarose gel was used to purify the gene, and a T4 DNA rapid ligation kit (Roche) was used to ligate the **H8** gene with previously *Nde*I/*Hin*dIII doubly digested pET-17b vector.

Purified **H8** cDNA served as the template for the **H9x** mutant, with two additional mutations, K86Q and C130S. These mutations were made in a stepwise fashion using the QuickChange site-directed mutagenesis kit (Stratagene). Primers used for mutagenesis of **H8** to create the **H9x** mutant are as follows: K86Q (forward) 5′, CCTGCAGGACATCCAAAAGCCGGATC; K86Q (reverse) 5′, GATCCGGCTTTTGGATGTCCTGCAGG; C130S (forward) 5′, CGACCCACATCTGTCTGATTTCATCGAAAC; C130S (reverse) 5′, GTTTCGATGAAATCAGACAGATGTGGGTCG. All sequences were confirmed by the University of Pennsylvania DNA Sequencing Facility in the School of Medicine.

Protein Expression and Purification. **wtH**, **H4**, **H8**, and **H9x** were transformed into *Escherichia coli* BL21-Codon Plus (DE3)-RP competent cells (Stratagene). Ten milliliter LB starter cultures (100 μg/mL ampicillin) were inoculated from single colonies and grown overnight at 37 °C, with shaking at 225 rpm. These cultures were then used to inoculate 1 L LB cultures (containing 200 μg/mL ampicillin) and grown until an $OD_{600} \sim 0.6-0.8$ was achieved. The cells were induced with 1 mM IPTG for 4 h. Cells were pelleted by centrifugation (5000 rpm, 20 min). The pellets were stored at −20 °C until use.

Purification was performed using a modified procedure by Levi et al. (*50*). Cell pellets were redissolved in 20 mM Tris and 0.15 M NaCl buffer at pH 7.4 (TBS), and a protease inhibitor cocktail tablet (Roche) was added. Cells were lysed on ice by sonication (3 × 2 min) and centrifuged (5000 rpm, 30 min). The lysis supernatant was heat shocked at 70 °C for 10 min and centrifuged (5000 rpm, 30 min). Ammonium sulfate (520 g/L) was added (*51*), stirred at 4 °C until all the ammonium sulfate dissolved, and centrifuged (5000 rpm, 30 min), and the pellet was redissolved in minimal TBS. The protein was run through a Superdex 200 10/300 GL column multiple times to remove other protein and DNA. Protein purity of >95% was confirmed by FPLC, SDS−PAGE gel electrophoresis, and UV−vis spectroscopy. Iron was removed using 2,2′-dipyridyl following the procedure of Levi et al. (*52*). Overall yields of iron-free apoferritin were 2 mg/L of LB for **wtH** and **H4** and 5 mg/L for **H8** and **H9x**, as determined by Bradford assay. Only pure ferritin was used for the studies presented in this paper.

Table 1: Characterization of Wild-Type and Designed Ferritin Proteins

protein	M_w (calc)	M_w (exptl)	DLS (radius, nm)	$[GuHCl]_{1/2}$ (M)	T_m (°C)
wtH	21226	21336	6.7	4.0	83
H4[a]	21085	21066	6.3	6.2	90
H8[b]	20982	20982	6.4	4.7	80

[a] **wtH** with H13D, C90R, C102A, and H105Q mutations. [b] **wtH** with H13D, C90R, C102A, H105Q, E64C, E140C, K143C, and E147C mutations.

Protein Characterization. Ferritin samples were analyzed by UV−vis spectroscopy with an Agilent 8453 spectrophotometer with temperature controller and magnetic stirrer (Agilent 89090A), using a quartz cuvette with 1 cm path length. The molecular weights of the ferritin four-helix bundle subunits were determined at the Wistar Institute Proteomics Facility using an Applied Biosystems Voyager System 6030 MALDI-TOF mass spectrometer and by SDS−PAGE using a 15% denaturing gel with SDS−PAGE broad range molecular weight standard (Bio-Rad). CD spectra were collected on an Aviv 62DS spectropolarimeter in the wavelength range 190−260 nm (far-UV) using a 1 mm quartz cell. Standard buffer is defined as 50 mM phosphate and 50 mM NaCl at pH 7.5.

Samples for thermal denaturation were prepared with 0.1 mg/mL protein in standard buffer. Ellipticity was measured at 222 nm by CD, and the temperature was increased from 4 to 96 °C in 2 °C steps. Samples were allowed to equilibrate for 1 min at each temperature. The melting process resulted in loss of signal as secondary structure was lost and the protein precipitated from solution. Melting temperatures were determined from the maximum of the first derivative plot of percent unfolded vs inverse temperature.

Samples for GuHCl denaturation were prepared with 0.1 mg/mL protein and concentrations of GuHCl varying between 0 and 7 M in standard buffer. The samples were mixed by vortex and allowed to stand at room temperature for 24 h, in order to achieve equilibrium at each guanidine concentration. The ratio of Trp fluorescence ($I_{316\,nm}/I_{360\,nm}$) was determined with a Varian Cary Eclipse fluorescence spectrophotometer operated with the Cary Eclipse Bio software package, upon excitation at 295 nm.

DLS was performed on a DynaPro instrument (Wyatt Technology Corp.), and the resulting data were analyzed with DYNAMICS Version 6.7. Samples were centrifuged at 15000 rpm for 10 min prior to measurement. A 5% intensity cutoff was applied to the data to compensate for fluctuations in signal. The polydispersity was less than 25% for all samples. Protein characterization data are summarized in Table 1.

Metal Binding, Nanoparticle Synthesis, and Characterization. Experiments were performed to determine the stoichiometry of Ag^+ binding to 24-mer apo**H4** and apo**H8**. Protein

Table 2: Data Collection and Refinement Statistics for Crystal Structure Determination of **H8** and Complexes Hg^{2+}−**H8** and Au^{3+}−**H9x**

	H8	Hg^{2+}-**H8** complex	Au^{3+}-**H9x** complex
PDB codes	2Z6M	3ERZ	3ES3
Data Collection			
resolution, Å	50.0−2.72	29.0−3.06	50.0−2.80
unique reflections	75646	47331	6736
R_{merge}[a]	0.096 (0.40)[b]	0.144 (0.37)[b]	0.128 (0.38)[b]
completeness (%)	99.0 (98.7)[b]	88.0 (91.7)[b]	98.8 (96.2)[b]
$I/\sigma(I)$	8.8 (1.9)[b]	9.6 (2.7)[b]	14.1 (3.2)[b]
multiplicity	3.6 (3.4)[b]	4.1 (4.0)[b]	5.1 (4.1)[b]
Refinement			
reflections used in refinement/test set	73383/3449	46055/1895	6325/243
R/R_{free}[c]	0.216/0.252	0.200/0.256	0.222/0.275
protein monomers[d]	12	12	1
water molecules[d]	368	207	52
Hg^{2+} ions[d]		12	
Ca^{2+} ions[d]	4	3	2
Zn^{2+} ions[d]	5	5	
Au^{3+} ions[d]			4
MPD molecules[d]	6	11	
rms Deviations			
bond lengths, Å	0.007	0.007	0.006
bond angles, deg	1.2	1.1	0.9
average *B*-factors, Å^2			
main chain	33	35	26
side chain	34	37	26
waters	29	29	27

[a] $R_{merge} = \sum|I - \langle I\rangle|/\sum I$, where I is the observed intensity and $\langle I\rangle$ is the average intensity calculated for replicate data. [b] Numbers in parentheses refer to the outer 0.1 Å shell of data. [c] Crystallographic *R*-factor, $R = \sum(|F_o| - |F_c|)/\sum|F_o|$, for reflections contained in the working set. $R_{free} = \sum(|F_o| - |F_c|)/\sum|F_o|$ for reflections contained in the test set excluded from refinement. $|F_o|$ and $|F_c|$ are the observed and calculated structure factor amplitudes, respectively. [d] Per asymmetric unit.

(0.2 mg/mL) in 50 mM MOPS buffer, pH 7.5, was titrated with aliquots of 10 equiv of Ag^+ at 60 s intervals and monitored by UV−vis spectroscopy at 25 °C with stirring at 300 rpm. No protein loss was observed during this loading procedure. A difference spectrum (Ag^+−protein minus protein in solution) was obtained for each sample, in order to observe the thiolate-to-silver charge-transfer band (*53*). The associated absorption change at 291 nm was averaged over three data sets. The number of silver atoms binding to **H4** and **H8** was calculated by finding the intersection point of straight lines fitted to the two different slopes. Error analysis was performed with a 1σ confidence limit using Igor Pro 5 (WaveMetrics, Inc.).

For nanoparticle synthesis, 1000 equiv of $AgNO_3$ or 2000 equiv of $AuCl_3$ was added to 0.2 mg/mL protein in 50 mM MOPS buffer at pH 7.5 and allowed to react for 18 h under a 60 W light (for Ag particle formation) or for 1.5 h on the benchtop (for Au particle formation). The protein−nanoparticle solutions were then centrifuged (10000 rpm, 10 min) to remove any large metal particles and further purified by passage through a 10-DG column (Bio-Rad). The protein−nanoparticle solutions were checked by UV−vis spectroscopy for the characteristic SPR bands (Ag, ~410 nm; Au, ~530 nm) to confirm reaction. Metal nanoparticles were characterized using ICP-OES by Galbraith Laboratories, Inc. Low-resolution TEM was performed at the University of Pennsylvania School of Medicine Biomedical Imaging Core.

Crystal Structure Determination for **H8.** **H8** was crystallized by the hanging drop vapor diffusion method at 21 °C. Typically, a drop containing 2.5 μL of protein solution (11.0 mg/mL **H8** in unbuffered 3.0 mM NaN_3) and 2.5 μL of precipitant buffer [0.1 M sodium acetate (pH 4.6), 20% (v/v) 2-propanol, 0.2 M $CaCl_2$] were equilibrated against a 1 mL reservoir of precipitant buffer. Crystals with a cubic morphology appeared within 2 days and grew to typical dimensions of 0.4 mm × 0.4 mm × 0.4 mm. These crystals diffracted to ~2.5 Å resolution on the home X-ray source, but persistent streaks were visible in all oscillation images that prevented data processing. A similar problem was encountered in the structure determination of bullfrog M ferritin and was attributed to the intrinsic disorder of ferritin molecules in the crystal (*54*). However, refinement of the **H8** crystallization conditions by altering the protein/precipitant drop ratio to 2.5 μL/1.0 μL yielded crystals with diamond-like morphology that were suitable for data collection. These crystals grew to typical dimensions of 0.2 mm × 0.2 mm × 0.1 mm within 4 days. To prepare the Hg^{2+}−**H8** complex, crystals of **H8** were gradually transferred to 100 mM sodium acetate (pH 4.6), 20% (v/v) 2-propanol, and 20 mM thimerosal and soaked for 10 days. During this time crystals were washed twice with the same solution containing 20 mM thimerosal.

Crystals of **H8** were cryoprotected by adding 2-methyl-2,4-pentanediol (MPD) to the mother liquor [final concentration = 45% (w/v)] and yielded diffraction data to 2.72 Å resolution at the Brookhaven National Laboratory (beamline X29A, λ = 1.0399 Å, 100 K). Data were processed with HKL-2000 (*55*) and scaled with SCALEPACK (*55*) (Table 2). Diffraction intensities measured from these crystals exhibited symmetry consistent with Laue group *P*422 (unit cell parameters $a = b = 171.3$ Å, $c = 190.5$ Å). Analysis of reflection conditions suggested the space group *P*422 or $P42_12$. Crystals of Hg^{2+}−**H8** were cryoprotected with a solution containing 45% (w/v) MPD and 0.1 M sodium acetate (pH 4.6) and yielded diffraction data to 3.06 Å resolution at the Brookhaven National Laboratory (beamline X29A, λ = 1.0399 Å, 100 K, unit cell parameters $a = b =$ 171.2 Å, c = 190.4 Å). Due to the small size of the Hg^{2+}−**H8** crystals, soaking experiments, and the high flux of the synchrotron beam, moderate crystal damage affected

data collection with an increased mosaicity of ~0.2°, which likely contributed to the relatively high R_{merge} value of 0.144.

The Matthews coefficient of 2.76 Å^3/Da (solvent content = 55.5%) indicated that the asymmetric unit of **H8** crystals contained 12 **H8** monomers. The crystal structure of **H8** was solved by molecular replacement with the program Phaser (*56*) using a hexamer of human ferritin as a search probe (PDB accession code 2FHA, less ions and water molecules) (*48*). The correct space group of **H8** crystals was determined to be $P42_12$ based on the fact that only with this space group were very strong peaks found for the translation function with correspondingly high values of log-likelihood gain (LLG) (*57*). Using data in the 23−3.2 Å resolution range, the optimal solution for the positioning of two hexamers in the asymmetric unit yielded a total LLG of 6304, RFZ = 14.8 and TFZ = 49.9 for the position of the first hexamer and RFZ = 17.3 and TFZ = 74.6 for the second hexamer. The Eulerian angles for the orientations of the two hexamers were $\alpha = 135.2°$, $\beta = 44.9°$, $\gamma = 89.9°$ and $\alpha = 287.2°$, $\beta = 90.0°$, $\gamma = 90.0°$, respectively, and the corresponding translational searches yielded $x = 0.53$ Å, $y = 0.23$ Å, $z = -0.30$ Å and $x = -86.3$ Å, $y = 0.32$ Å, $z = 89.8$ Å. The packing of the two hexamers in the asymmetric unit yielded a 24-mer assembly with 432 point group symmetry by the application of the symmetry operators for space group $P42_12$.

Iterative cycles of model building with the graphics program O (*58*) and refinement against 50.0−2.72 Å resolution data using torsion angle dynamics as implemented in CNS (*59*) improved the protein structure, as monitored by the values of R and R_{free}. A restrained noncrystallographic symmetry was used during all refinement processes with an appropriate weighting scheme (CNS) as judged by R_{free} and the residual Fourier map as refinement progressed. Group B-factors were utilized during refinement, and the majority of water molecules were automatically fit into residual electron density peaks using a cutoff of 3.0σ, which improved the R and R_{free} values to those reported in Table 2. A total of 368 water molecules was included in the refinement. Strong peaks aligned on the 3-fold axes located 2.2−2.9 Å from E131/E134 were modeled as Ca^{2+} ions from the crystallization medium. Additional strong peaks aligned on the 4-fold axes located 3.1 Å from H173 of the terminal E-helices were tentatively identified as Zn^{2+} ions based on inspection of the Bijvoet difference Fourier map calculated with anomalous data collected at the wavelength corresponding to the Zn edge. Disordered segments at the N- and C-termini (M1−S4 and D177−S182) were absent in the experimental electron density and are omitted from the final model.

The crystal structure of Hg^{2+}−**H8** was solved by the difference Fourier method and refined as described for the structure of **H8** with exception that in later cycles the refinement was completed with PHENIX (*60*). Strong peaks were observed in the simulated annealing map and identified as mercury ions. Disordered segments at the N- and C-termini (M1−S4 and D177−S182) were absent in the experimental electron density and are omitted from the final model. During refinement process we noted in the residual Fourier map a broad ~5σ peak adjacent to C64. This peak was ambiguous but may correspond to disordered thimerosal or MPD from the crystallization medium.

Crystal Structure Determination for **H9x.** Crystals of **H9x** were prepared in a similar manner as described for **H8**, and the Au^{3+}−**H9x** complex was prepared by soaking crystals in a solution of 0.5 mM $AuCl_3$ of mother liquor with the absence of Ca^{2+} for 1 week. X-ray diffraction data were collected from crystals of the Au^{3+}−**H9x** complex at the Cornell High Energy Synchrotron Source (CHESS) on beamline A1a and diffracted to 2.80 Å resolution. These crystals were isomorphous (space group $F432$, $a = 181.6$ Å) with the cubic crystal structure of human H chain ferritin (Table 2).

The crystal structure was solved by molecular replacement using the monomer from the **H8** structure as a search probe for rotation and translation functions. The structure was refined as described above with the exception that in the latter cycles the refinement was completed with PHENIX (*60*). Strong peaks were observed in the simulated annealing map and identified as Au^{3+} ions.

RESULTS

Computational Design. Exterior Cys and His residues were targeted for mutation, so as to minimize protein aggregation and nanoparticle nucleation at the protein outer surface. Cysteines and histidines are excellent ligands for noble metal ions. Furthermore, C90 and C102 were shown previously to promote ferritin aggregation through sulfur oxidation chemistry (*61*). Thus, calculations were performed to help identify optimal replacements for C90, C102, H13, and H105.

Probabilistic computational design methods were used to determine the likelihoods of the amino acids at these positions. The most probable residue at site 90 was Arg. The resulting model structure suggested that the guanidinium group of R90 can hydrogen bond with the backbone oxygen of D92 and form a salt bridge with E94. The most probable amino acids at site 102 were Ser and Ala. Alanine was selected due to its inertness toward metal binding, high α-helix propensity, and proximity to nearby hydrophobic residues (Trp93 and Met37). At position 13 on the protein exterior, Asp was the most probable residue, stabilized by a potential interhelical salt bridge with K124. For site 105, Glu, Lys, and Gln were preferred and had comparable probabilities. The wild-type crystal structure suggested that an ionizable residue at site 105 may disrupt a network of hydrogen-bonding and ionic interactions involving K109, Q7, R9, E101, and R156. The neutral H105Q mutation was selected to minimize interference with these wild-type interactions.

Calculations were also performed to identify interior sites where cysteines could be stably incorporated so as to promote metal ion binding and nanoparticle formation within the protein cavity. Site 135 exhibited a strong preference for the wild-type residue, particularly at low energies, and as a result Thr was retained at this position. At each of the four remaining sites (E64, E140, K143, E147), Cys had a probability comparable to the wild-type residues: E64, $P_{Cys}/P_{wt} = 2.0$; E140, $P_{Cys}/P_{wt} = 1.3$; K143, $P_{Cys}/P_{wt} = 0.5$; E147, $P_{Cys}/P_{wt} = 0.4$. Note that cysteines at sites 143 and 147 are less probable than wild type, suggesting that these mutations could destabilize the protein.

Biophysical Characterization. Upon expression and purification, the three proteins were studied for their assembly and stability. Dynamic light scattering (DLS) measurements indicated that **H4** and **H8** had virtually identical hydrody-

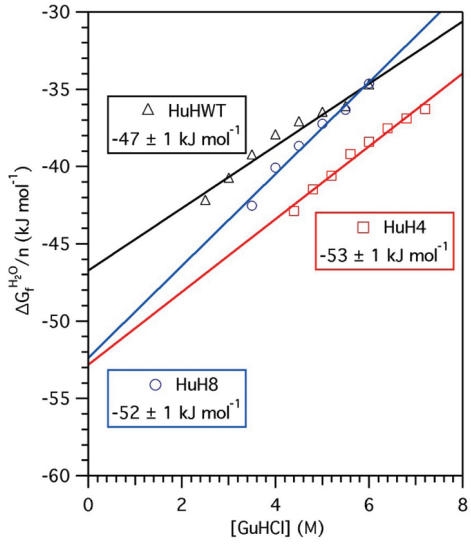

FIGURE 1: Free energy of folding dependence of **wtH**, **H4**, and **H8** as a function of GuHCl concentration calculated on a per subunit basis, $n = 24$. Linear extrapolation to 0 M GuHCl yielded $\Delta G_f^{H_2O}$ per mole of subunit in the absence of denaturant. Least-squares fitting was used to obtain the solid lines.

namic radii to **wtH**. Each protein had a similar retention time by size exclusion chromatography (Figure S1, Supporting Information). Minimal 24-mer aggregation was observed for both **H4** and **H8** as shown by the disappearance of peaks corresponding to trimer (3 × 24-mer, elution at ~8 mL) and dimer (2 × 24-mer, elution at ~9 mL) with **wtH**. Multimerization of the 24-mer has been observed in other ferritins such as HSAF (*62*). **H4** and **H8** were more stable to guanidine denaturation than **wtH** (Table 1, Figure S2, Supporting Information), as monitored by tryptophan fluorescence that red shifted upon ferritin disassembly. Thermal denaturation experiments, in which loss of α-helical content at 222 nm was monitored by CD spectroscopy, determined the T_m (Figure S3, Supporting Information). The free energy of folding was calculated for **wtH** (−47 kJ·mol^{-1}), **H4** (−53 kJ·mol^{-1}), and **H8** (−52 kJ·mol^{-1}) as previously described (Figure 1) (*31*).

H8 *X-ray Crystallography.* The X-ray crystal structure of **H8** (Figure 2, PDB code 2Z6M) confirmed proper assembly of the 24-mer holoprotein. Interestingly, a tetragonal crystal form resulted, which was the first time HuHF has been crystallized without the K86Q mutation. This crystal form was previously observed for horse spleen ferritin (but not for any human ferritin) with different unit cell parameters ($a = b = 147.2$ Å, $c = 152.6$ Å; PDB accession code 1IES) (*63*). The **H8** structure was refined to final R and R_{free} values of 0.215 and 0.252, respectively (Table 2). The root-mean-square deviation of 172 C_α atoms between **H8** and wild type (PDB code 2FHA) (*48*) was 0.38 Å, indicating close structural homology. The cysteines in the cavity remained reduced under the conditions employed for crystallization. Electron density maps showing some of the engineered cysteine residues and the Zn^{2+} binding site are shown in Figure 3.

Silver and Gold Nanoparticle Synthesis. Ag^+ titrations were performed with 0.2 mg/mL **H8** and monitored by UV−vis difference spectroscopy to determine the accessibility of cysteines within the protein interior. Absorbance at 291 nm may be assigned to a thiolate → Ag(I) charge-transfer band (Figure 4) (*53*). These data were consistent with **H4** containing 1.0 ± 0.8 Cys per subunit (C130, located in the 3-fold symmetric pores) and **H8** containing 4.3 ± 2.9 cysteines per subunit (four designed Cys mutations and C130). **H4** serves as a useful control in these experiments, as the only difference between **H4** and **H8** is the incorporation of 96 cysteine residues within the **H8** interior. These experiments indicate that cysteines introduced within the cavity are largely accessible to Ag^+ ions in solution.

Silver nanoparticles were synthesized by adding 1000 equiv of $AgNO_3$ to each apoferritin sample (0.2 mg/mL in 50 mM MOPS buffer, pH 7.5) and stirring at room temperature for 18 h while illuminating (60 W bulb, equivalent to 10 mW/cm^2 over the visible range, measured at the sample). All reactions with **wtH**, **H4**, and **H8** turned yellow-brown within several hours. However, only the silver−**H8** sample remained intensely yellow after centrifugation and elution through a gel filtration column and also exhibited a typical SPR band for silver nanoparticles, $\lambda_{max} = 412$ nm (Figure 5). In MOPS buffer alone and in protein solutions that were not exposed to light, no color change was observed after 18 h, which confirmed that both the protein and light were required to form silver particles. The centrifugation and gel filtration purification steps ensured the removal of bulk silver.

In reactions of **H8** with Au^{3+}, reduction by MOPS buffer gave a characteristic gold SPR band at 534 nm (Figure 6). In the absence of MOPS, with only protein in solution to reduce the Au^{3+} ions, gold nanoparticles were observed to form on the time scale of weeks instead of minutes. The SPR max of the **Au**−**H8** sample was slightly red-shifted compared to **Au**−**wtH** and **Au**−**H4**. While **wtH** and **H8** appeared to stabilize Au^0 in solution, **Au**−**H4** appeared to

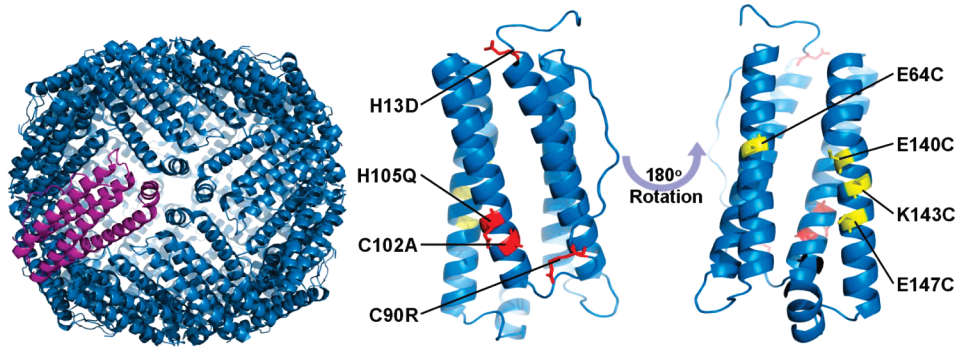

FIGURE 2: X-ray crystal structure (2.72 Å resolution) of a designed human H ferritin (**H8**) expanded to show a single **H8** four-helix bundle subunit with mutations made to the exterior (red) and interior (yellow) surfaces.

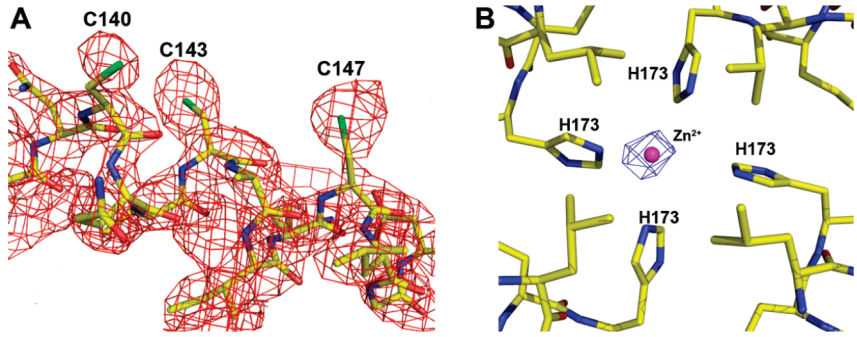

FIGURE 3: X-ray crystal structure (2.72 Å resolution) of a designed human H ferritin (**H8**) soaked with Zn^{2+}. (A) Simulated annealing omit electron density map for the segment L138−G149 in which the three residues mutated to cysteines are indicated. (B) Bijvoet difference Fourier map calculated with anomalous data collected at a wavelength corresponding to the Zn edge, contoured at 3.2σ.

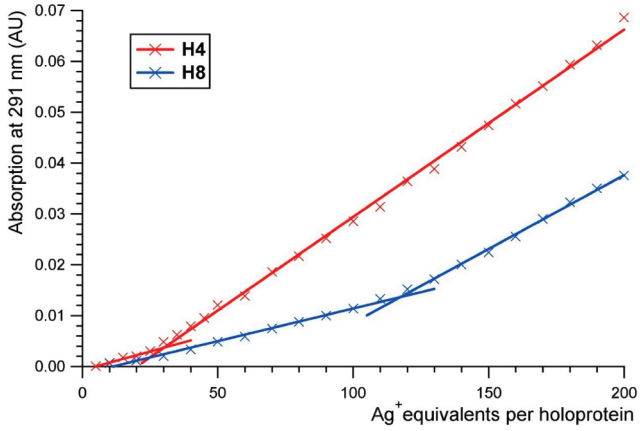

FIGURE 4: Difference spectra of Abs_{291} vs Ag^+ equivalents, where the initial slope reports Cys−Ag^+ interaction in **H4** and **H8** and the steeper slope likely reflects less discriminate binding between additional equivalents of Ag^+ and metal-binding residues on the two mutants. The two best-fit lines are consistent with a two-classes-of-sites binding model.

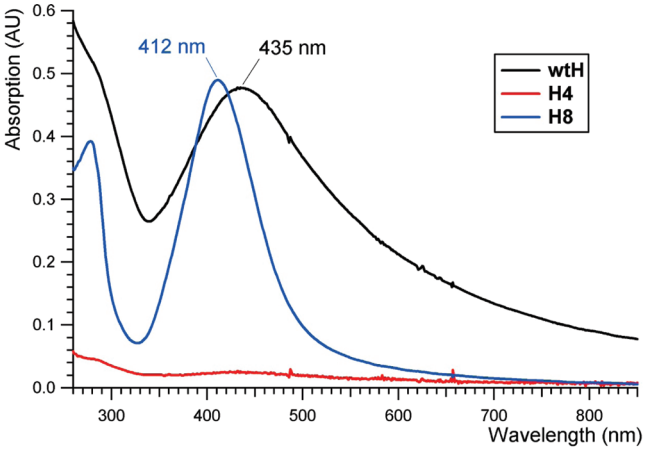

FIGURE 5: UV−vis spectra of **wtH**, **H4**, and **H8**, each reacted with 1000 equiv of Ag^+, reduced with MOPS and light, and centrifuged at 10000 rpm for 10 min. SPR absorbance peaks are labeled. Proteins (0.2 mg/mL) in 50 mM MOPS, pH 7.5.

aggregate based on the elevated baseline compared to the other two samples. Such aggregation with **H4** was not unexpected and is likely the result of fewer Au^0−surface interactions in **H4** compared to **wtH**.

Loading of **H8** with silver or gold was examined under various reaction conditions. The described procedures were performed dozens of times over many months for each protein−metal combination and gave very reproducible

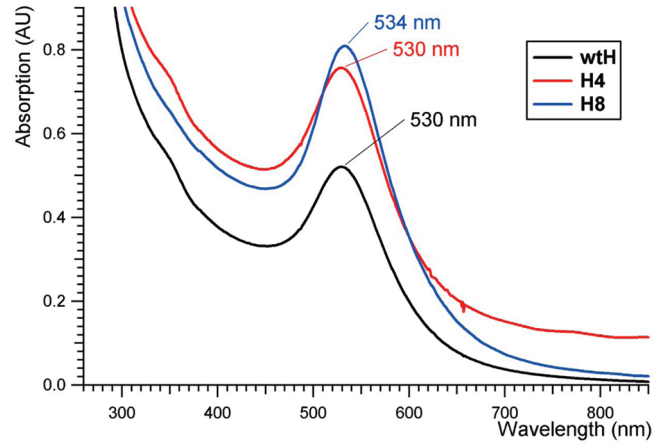

FIGURE 6: UV−vis spectra of 0.2 mg/mL **wtH**, **H4**, and **H8** after 90 min reaction with 2000 equiv of Au^{3+} in 50 mM MOPS, pH 7.5. Samples were centrifuged at 10000 rpm for 10 min, and buffer was exchanged to dd H_2O before spectra were taken. λ_{max}= 530 nm (**wtH** and **H4**) and λ_{max}= 534 nm (**H8**).

results. Based on Bradford assays using both BSA and ferritin standards, ∼50% of **H8** was retained in solution during metal particle synthesis. By comparison, 100% of the **H8** protein was retained during iron loading. According to ICP-OES, **Ag−H8** contained an average of 270 Ag atoms per holoprotein, which corresponded to uptake of 27% of available silver in solution under these reaction conditions. ICP-OES showed that **H8** contained an average of 440 Au atoms per holoprotein, indicating that **H8** was able to uptake 22% of available gold under these reaction conditions. Based on TEM images for the **Au−H8** samples, a small number of gold particles larger than the ferritin cavity were retained postpurification. Thus, the loading number obtained via ICP-OES for the gold samples should be considered an upper limit for these experiments. The 2−4 nm diameter cores of Ag^0 and Au^0 observed in many ferritin shells by TEM were consistent with spherical clusters of 300−2000 atoms.

Fe-Loaded **H8.** Iron-loading experiments with **H8**, monitored by UV−vis spectroscopy, showed ferric oxide−mineral formation upon addition of 2000 equiv of Fe^{2+} (data not shown). ICP-OES performed on these samples indicated 1800 equiv of iron (>90% incorporation) per **H8** 24-mer, as expected for an iron-mineralized ferritin protein. TEM images of iron mineral−**H8** (**Fe−H8**) showed a white outer protein shell and darker inner metallic core (Figure 7), which appeared very similar to the **Ag−H8** and **Au−H8** TEM images. Similarities in TEM data between **Fe−H8**, where the mineral occupies the cavity, and **Ag−H8** and **Au−H8**

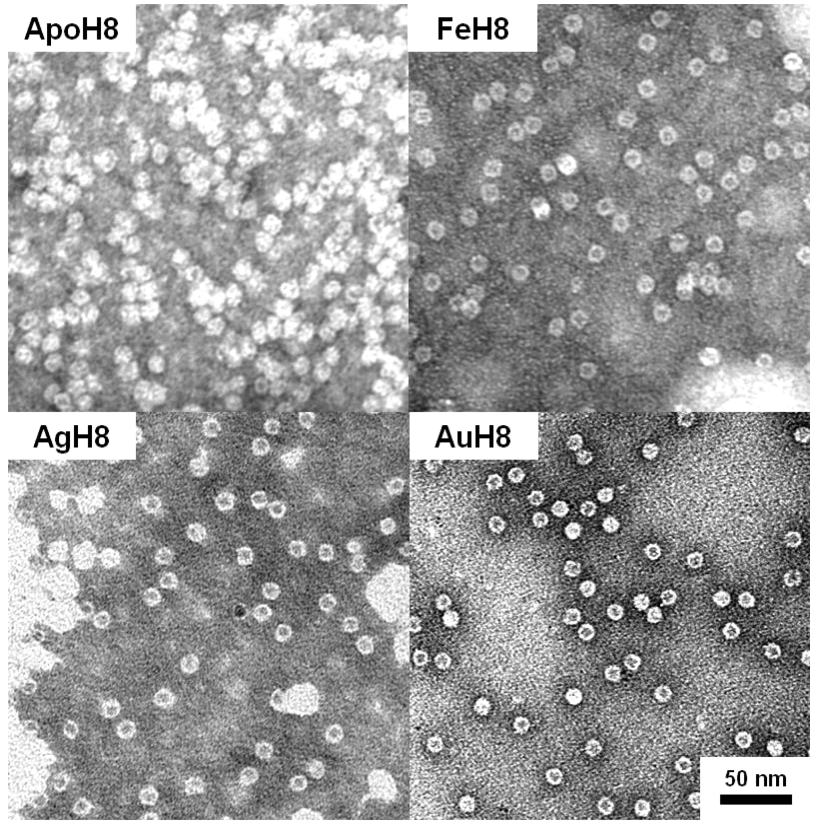

FIGURE 7: TEM images of 0.2 mg/mL apo**H8** alone and apo**H8** reacted with 2000 equiv of Fe^{2+} in the presence of ambient dioxygen, 1000 equiv of Ag^{+}, or 2000 equiv of Au^{3+} showing protein (white 12 nm diameter spheres counterstained with 0.2% uranyl acetate) and ferric hydroxide, Ag^{0} or Au^{0} cores.

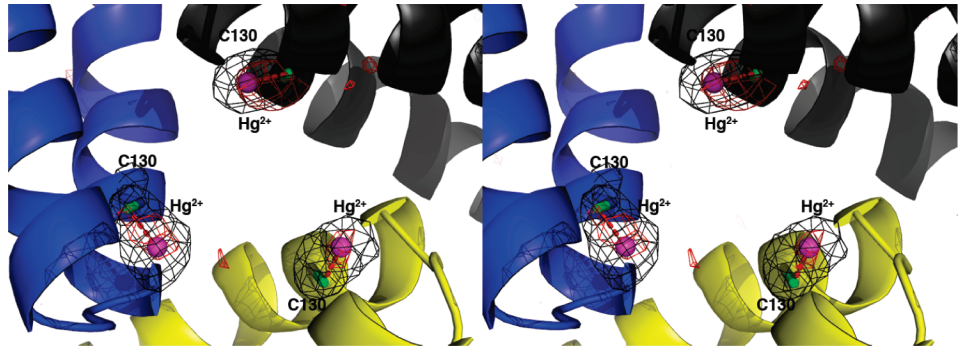

FIGURE 8: Crystal structure of the Hg^{2+}−**H8** complex (3.06 Å resolution) with view of the 3-fold symmetric channel: C130−Hg^{2+} coordination interactions (red dashed lines) at the interior mouth of the 3-fold channel formed by monomers G, K, and I (blue, gray, and yellow, respectively). The sulfur atoms of C130 are in green and the Hg^{2+} ions are in magenta. Simulated annealing omit electron density map for the Hg^{2+} ions calculated with coefficients $|F_o| - |F_c|$, contoured at 5σ (black). Bijvoet difference Fourier map calculated with anomalous data collected at a wavelength corresponding to the Hg edge and the phases from the refined model less the atoms of Hg^{2+}, contoured at 3σ (red). Mercury occupancies are estimated to be 50%.

provided strong evidence that mutations made to the HuHF exterior and interior surfaces promoted silver and gold nanoparticle formation inside the protein cavity.

*Hg^{2+}−**H8** X-ray Crystallography.* To examine why higher levels of noble metal loading were not observed in **H8**, Au^{3+} soaks with protein crystals were attempted. Unfortunately, the presence of the gold ions caused crystal diffraction to appear mosaic, and Ag^{+} was characteristically insoluble under protein crystallization conditions. Hg^{2+} was then used instead to probe metal−thiol interactions. The Bijvoet difference Fourier map calculated with anomalous data collected at a wavelength corresponding to the Hg edge confirms the identities of the mercury ions coordinated to the C130 (2.3−2.5 Å) at the entrance of the channel aligned with the 3-fold axes (Figure 8). The Hg^{2+} ions were refined with an occupancy estimated to be 0.5 corresponding to an average thermal (*B*) factor of 68 $Å^2$, indicative of partial disorder (Table 2).

*Au^{3+}−**H9x** X-ray Crystallography.* Preliminary studies were performed to explore noble metal loading in the absence of C130, by making two mutations to **H8** to create a new HuHF protein, **H9x**. The first mutation, K86Q, was done for previous HuHF crystal structures (PDB codes 1FHA and 2FHA) (*48, 64*), in order to improve ferritin intermolecular contacts, crystal growth, and diffraction. This exterior mutation should have little effect on noble metal binding. The second mutation was replacement of C130 with serine, as this residue should be less reactive with Au^{3+} but is

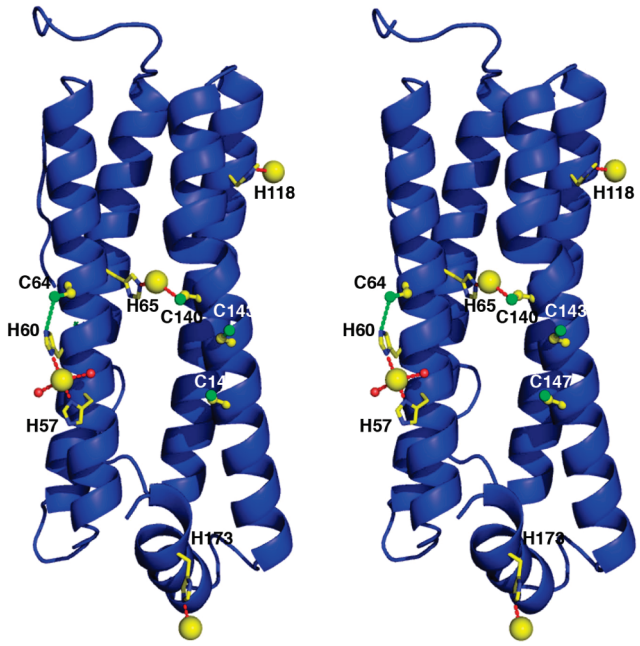

FIGURE 9: Crystal structure of Au^{3+}−**H9x** complex (2.80 Å resolution). The Bijvoet difference Fourier map for Au^{3+}−**H9x** calculated with anomalous data collected at the wavelength near to the gold edge identified the gold ion coordinated to C140 and three additional peaks identified as gold coordinated to histidines (H57 and H60, H118, and H173). Three of four gold ions were refined with partial occupancy, and the total average thermal *B*-factor for gold ions is 50 $Å^2$. Significantly, the side chains of H60 and H57 undergo conformational changes with respect to the **H8** structure in order to coordinate the gold ion.

isosteric with and similarly polar to cysteine. The C130S mutation should minimally perturb the integrity of the 3-fold channel.

In the crystal structure of **H9x** soaked with $AuCl_3$, no gold ions were observed within the 3-fold symmetric channels, whereas gold ions were indeed observed at engineered cysteines in the **H9x** interior (Figure 9). This provides additional evidence that mutations made to surface-accessible residues (i.e., C130) can help to direct metal ions to the HuHF interior. Notably, however, in studies of gold and silver nanoparticle formation, UV−vis spectroscopy, TEM, and ICP-OES gave very similar data for **H8** and **H9x**. Thus, additional factors controlling noble metal ion loading, reduction, nanoparticle formation and stabilization remain to be identified in this system.

DISCUSSION

Biophysical Results. Relative to **wtH**, the designed exterior mutations stabilized the protein (Figure 1, Table 1). The increase in **H4** stability relative to **wtH** is most likely due to removal of the surface cysteines, which have been shown to cause ferritin aggregation (*61*), and introduction of stabilizing interactions involving surface exposed residues (C90R, H13D). With its 192 mutations guided by SCADS, it is remarkable that **H8** exhibits nearly identical stability to **H4** in solution despite the added interior cysteine residues.

Silver and Gold Nanoparticle Synthesis. The red-shifted Ag^0 SPR band seen for **wtH** (λ_{max} = 435 nm, with elevated baseline, Figure 5) is attributed to particle aggregation and partial solubilization of Ag^0 via interactions with external Cys and/or His residues. Similar phenomena were seen previously in our laboratory with silver nanoparticle−HSAF assemblies (data not shown) and are similar to results observed with HSAF by Dominguez-Vera using $NaBH_4$ as the reducing agent (*21*).

H4, which had the external Cys and His residues removed, serves as a useful control in these experiments, to allow direct comparison of the wild-type and cysteine-engineered protein interiors. **H4** shows almost no SPR band, which indicates that **H4** is unable to stabilize the silver particles that form in solution to the purification steps of centrifugation and gel filtration. In contrast, the purified **Ag−H8** sample remains intensely yellow and exhibits a typical SPR band for silver nanoparticles, λ_{max} = 412 nm. These data indicate that the cysteine-rich cavity is critical in forming stable silver nanoparticles at the protein interior. The removal of Cys and His residues from the protein exterior appears to favor reaction at these internal sites.

For the Au loading studies, clear differences are also observed between **wtH**, **H4**, and **H8**. **H4** shows scattering (elevated baseline, Figure 6), which is indicative of poor particle solubilization, and results from the removal of exterior cysteine and histidine residues. **wtH** gives a characteristic SPR for gold, which indicates that the exterior wild-type surface (with particular emphasis on cysteine and histidine) stabilizes gold nanoparticles in solution as we saw previously for HSAF (*22*). However, the intensity of the Au SPR band is much greater for **H8**, providing evidence that a higher concentration of gold nanoparticles are stabilized in solution when grown within the protein interior.

X-ray Crystallography. As shown in Figure 8, the primary binding sites for the Hg^{2+} ions were the Cys130 residues at the interior opening of the 3-fold pore. While it is believed that C130 helps to facilitate metal ion transport into the protein, soft metal ions binding to these residues at the 3-fold pore, and subsequent reduction, could slow uptake and limit metal loading. Although there is no direct evidence for C130 nucleating gold and silver nanoparticle formation, reaction at this site has the potential to block the 3-fold channels and limit the size of the particles formed. Support for this hypothesis is provided by a crystal structure of **H9x** (Figure 9), in which C130 is replaced with serine, and Au ions soaked with the protein are observed at engineered cysteines in the **H9x** interior.

Computational and Crystallographic Comparison. In Figure 10, we compare the **H8** structures determined via crystallographic refinement (Figure 2) with the calculated structures of the probable side chain conformational states. Each of the mutated sites is largely surface exposed, and a variety of populated side chain conformations may be expected. Nonetheless, the calculation yields local structure comparable to that observed in the experimentally determined structure, particularly with regard to C140 and C143 and the placement of the guanidinium group of R90. This comparison demonstrates the power of applying computation toward the design of ferritin proteins with new chemical reactivity.

In summary, variants of HuHF (**H4** and **H8**) were designed with Cys and His residues removed from the outer surface. **H8** also incorporated 96 non-native cysteines within the cavity, which was confirmed by X-ray crystallography. Both HuHF mutants formed very stable tetracosamers, but as designed, only **H8** templated the synthesis of water-soluble, nonaggregating Ag^0 and Au^0 nanoparticles within the protein

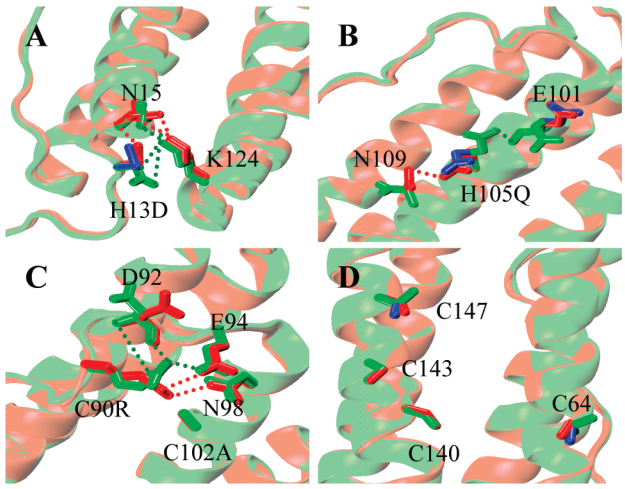

FIGURE 10: Side chain structural comparison of the eight mutation sites: X-ray crystallographically determined structure (red) and structure resulting from computational design (green). The exterior His deletions of H13D (A) and H105Q (B) and Cys deletions of C90R and C102A (C) are shown with main interresidue interactions. Side chain structures: X-ray crystal structure (red), the most probable rotamers (green), and the most similar rotamers to the X-ray structures (blue). The interior Cys conformations (D) are compared. In panel D, the blue sticks for Cys are the second most probable rotamer.

interior, as indicated by UV−vis and TEM data. As expected, **H4** was relatively ineffective at stabilizing silver and gold nanoparticles in solution, based on the lack of available ligands on its exterior and interior surfaces.

This work illustrates how accessible protein surfaces may be engineered to control metal ion binding and subsequent chemistries. Ferritins support the wide-scale mutagenesis of residues important in metal surface chemistry, and it has become evident that ferritin, with eight 3-fold symmetric channels, can provide a useful model for studying the transport of metal ions within protein frameworks. Lessons learned from controlling the chemistry of noble metals in ferritin may be applied to other biomolecularly templated inorganic structures.

ACKNOWLEDGMENT

The authors thank Paolo Arosio for providing the HuHF cDNA, Vijay Yerubandi for help with protein expression and purification, Neelima Shah and Ray Meade for TEM work, Roderic Eckenhoff for use of DLS equipment, and Feng Gai for use of the CD spectrometer.

SUPPORTING INFORMATION AVAILABLE

Figures S1−S3 providing FPLC traces, guanidine denaturation, and thermal denaturation curves for **wtH**, **H4**, and **H8**. This material is available free of charge via the Internet at http://pubs.acs.org.

REFERENCES

1. Kröger, N., Deutzmann, R., and Sumper, M. (1999) Polycationic peptides from diatom biosilica that direct silica nanosphere formation. *Science 286*, 1129–1132.
2. Porter, S. M. (2007) Seawater chemistry and early carbonate biomineralization. *Science 316*, 1302.
3. Dorozhkin, S., and Epple, M. (2002) Biological and medical significance of calcium phosphates. *Angew. Chem., Int. Ed. 41*, 3130–3146.
4. Manceau, A., Nagy, K. L., Marcus, M. A., Lanson, M., Geoffroy, N., Jacquet, T., and Kirpichtchikova, T. (2008) Formation of metallic copper nanoparticles at the soil-root interface. *Environ. Sci. Technol. 42*, 1766–1772.
5. Scheffel, A., Gruska, M., Faivre, D., Linaroundis, A., Plitzko, J. M., and Schüler, D. (2006) An acidic protein aligns magnetosomes along a filamentous structure in magnetotactic bacteria. *Nature 440*, 110–114.
6. Klaus, T., Joerger, R., Olsson, E., and Granqvist, C.-G. (1999) Silver-based crystalline nanoparticles microbially fabricated. *Proc. Natl. Acad. Sci. U.S.A. 96*, 13611–13614.
7. Lengke, M. F., Fleet, M. E., and Southam, G. (2007) Biosynthesis of silver nanoparticles by filamentous cyanobacteria from silver(I) nitrate complex. *Langmuir 23*, 2694–2699.
8. Ahmad, A., Sennapati, S., Khan, M. I., Kumar, R., and Sastray, M. (2003) Extracellular biosynthesis of monodisperse gold nanoparticles by a novel extremophilic actinomycete, *Thermomonospora* sp. *Langmuir 19*, 3550–3553.
9. Blum, A. S., Soto, C. M., Wilson, C. D., Cole, J. D., Kim, M., Gnade, B., Chatterji, A., Ochoa, W. F., Lin, T., Johnson, J. E., and Ratna, B. R. (2004) Cowpea mosaic virus as a scaffold for 3-D patterning of gold nanoparticles. *Nano Lett. 4*, 867–870.
10. Everts, M., Saini, V., Leddon, J. L., Kok, R. J., Stoff-Khalili, M., Preuss, M. A., Millican, C. L., Perkins, G., Brown, J. M., Bagaria, H., Nikles, D. E., Johnson, D. T., Zharov, V., and Curiel, D. T. (2006) Covalently linked Au nanoparticles to a viral vector: Potential for combined photothermal and gene cancer therapy. *Nano Lett. 6*, 587–591.
11. Joshi, H. M., Bhumkar, D. R., Joshi, K., Pokharkar, V., and Sastry, M. (2006) Gold nanoparticles as carriers for efficient transmucosal insulin delivery. *Langmuir 22*, 300–305.
12. Dominguez-Vera, J. M., and Colacio, E. (2003) Nanoparticles of Prussian blue ferritin: A new route for obtaining nanomaterials. *Inorg. Chem. 42*, 6983–6985.
13. Comotti, M., Pina, C. D., Matarrese, R., and Rossi, M. (2004) The catalytic activity of "naked" gold particles. *Angew. Chem., Int. Ed. 43*, 5812–5815.
14. Merga, G., Wilson, R., Lynn, G., Milosavljevic, B. H., and Meisel, D. (2007) Redox catalysis of "naked" silver nanoparticles. *J. Phys. Chem. C 111*, 12220–12226.
15. Schofield, C. L., Haines, A. H., Field, R. A., and Russell, D. A. (2006) Silver and gold glyconanoparticles for colorimetric bioassays. *Langmuir 22*, 6707–6711.
16. Li, Y., Wu, Y., and Ong, B. S. (2005) Facile synthesis of silver nanoparticles useful for fabrication of high-conductivity elements for printed electronics. *J. Am. Chem. Soc. 127*, 3266–3267.
17. Doty, R. C., Tshikhudo, T. R., Brust, M., and Fernig, D. G. (2005) Extremely stable water-soluble Ag nanoparticles. *Chem. Mater. 17*, 4630–4635.
18. Zheng, J., and Dickson, R. M. (2002) Individual water-soluble dendrimer-encapsulated silver nanodot fluorescence. *J. Am. Chem. Soc. 124*, 13982–13983.
19. Lesniak, W., Bielinska, A. U., Sun, K., Janczak, K. W., Shi, X., Jr., and Balogh, L. P. (2005) Silver/dendrimer nanocomposites as biomarkers: Fabrication, characterization, in vitro toxicity, and intracellular detection. *Nano Lett. 5*, 2123–2130.
20. Eriksson, A. E., Baase, W. A., Zhang, X. J., Heinz, D. W., Blaber, M., Baldwin, E. P., and Matthews, B. W. (1992) Response of a protein structure to cavity-creating mutations and its relation to the hydrophobic effect. *Science 255*, 178–183.
21. Dominguez-Vera, J. M., Gálvez, N., Sánchez, P., Mota, A. J., Trasobares, S., Hernández, J. C., and Calvino, J. J. (2007) Size-controlled water-soluble Ag nanoparticles. *Eur. J. Inorg. Chem. 30*, 4823–4826.
22. Zhang, L., Swift, J., Butts, C. A., Yerubandi, V., and Dmochowski, I. J. (2007) Structure and activity of apoferritin-stabilized gold nanoparticles. *J. Inorg. Biochem. 101*, 1719–1729.
23. Ueno, T., Suzuki, M., Goto, T., Matsumoto, T., Nagayama, K., and Watanabe, Y. (2004) Size-selective olefin hydrogenation by a Pd nanocluster provided in an apo-ferritin cage. *Angew. Chem., Int. Ed. 43*, 2527–2530.
24. Ensign, D., Young, M., and Douglas, T. (2004) Photocatalytic synthesis of copper colloids from Cu(II) by the ferrihydrite core of ferritin. *Inorg. Chem. 43*, 3441–3446.
25. Douglas, T., and Stark, V. T. (2000) Nanophase cobalt oxyhydroxide mineral synthesized within the protein cage of ferritin. *Inorg. Chem. 39*, 1828–1830.

26. Okuda, M., Iwahori, K., Yamashita, I., and Yoshimura, H. (2003) Fabrication of nickel and chromium nanoparticles using the protein cage of apoferritin. *Biotechnol. Bioeng. 84*, 187–194.
27. Pead, S., Durrant, E., Webb, B., Larsen, C., Heaton, D., Johnson, J., and Watt, G. D. (1995) Metal ion binding to apo, holo, and reconstituted horse spleen ferritin. *J. Inorg. Biochem. 59*, 15–27.
28. Kim, I., Hosein, H.-A., Strongin, D. R., and Douglas, T. (2002) Photochemical reactivity of ferritin for Cr(VI) reduction. *Chem. Mater. 14*, 4874–4879.
29. Yoshizawa, K., Iwahori, K., Sugimoto, K., and Yamashita, I. (2006) Fabrication of gold sulfide nanoparticles using the protein cage of apoferritin. *Chem. Lett. 35*, 1192–1193.
30. Kramer, R. M., Li, C., Carter, D. C., Stone, M. O., and Naik, R. R. (2004) Engineered protein cages for nanomaterial synthesis. *J. Am. Chem. Soc. 126*, 13282–13286.
31. Swift, J., Wehbi, W. A., Kelly, B. D., Fu Stowell, X., Saven, J. G., and Dmochowski, I. J. (2006) Design of functional ferritin-like proteins with hydrophobic cavities. *J. Am. Chem. Soc. 128*, 6611–6619.
32. Korkegian, A., Black, M. E., Baker, D., and Stoddard, B. L. (2005) Computational thermostabilization of an enzyme. *Science 308*, 857–860.
33. Kuhlman, B., Dantas, G., Ireton, G. C., Varani, G., Stoddard, B. L., and Baker, D. (2003) Design of a novel globular protein fold with atomic-level accuracy. *Science 302*, 1364–1368.
34. Topoglidis, E., Discher, B. M., Moser, C. C., Dutton, P. L., and Durrant, J. R. (2003) Functionalizing nanocrystalline metal oxide electrodes with robust synthetic redox proteins. *ChemBioChem 4*, 1332–1339.
35. Cochran, F. V., Wu, S. P., Wang, W., Nanda, V., Saven, J. G., Therien, M. J., and DeGrado, W. F. (2005) Computational *de novo* design and characterization of a four-helix bundle protein that selectively binds a nonbiological cofactor. *J. Am. Chem. Soc. 127*, 1346–1347.
36. Bender, G. M., Lehmann, A., Zou, H., Cheng, H., Fry, H. C., Engel, D., Therien, M. J., Blasie, J. K., Roder, H., Saven, J. G., and DeGrado, W. F. (2007) De novo design of a single-chain diphenylporphyrin metalloprotein. *J. Am. Chem. Soc. 129*, 10732–10740.
37. Calhoun, J. R., Kono, H., Lahr, S., Wang, W., DeGrado, W. F., and Saven, J. G. (2003) Computational design and characterization of a monomeric helical dinuclear metalloprotein. *J. Mol. Biol. 334*, 1101–1115.
38. Kaplan, J., and DeGrado, W. F. (2004) De novo design of catalytic proteins. *Proc. Natl. Acad. Sci. U.S.A. 101*, 11566–11570.
39. Looger, L. L., and Hellinga, H. W. (2001) Generalized dead-end elimination algorithms make large-scale protein side-chain structure prediction tractable: Implications for protein design and structural genomics. *J. Mol. Biol. 307*, 429–445.
40. Zou, J. M., and Saven, J. G. (2003) Using self-consistent fields to bias Monte Carlo methods with applications to designing and sampling protein sequences. *J. Chem. Phys. 118*, 3843–3854.
41. Park, S., Xi, Y., and Saven, J. G. (2004) Advances in computational protein design. *Curr. Opin. Struct. Biol. 14*, 487–494.
42. Kono, H., and Saven, J. G. (2001) Statistical theory for protein combinatorial libraries. Packing interactions, backbone flexibility, and the sequence variability of a main-chain structure. *J. Mol. Biol. 306*, 607–628.
43. Zou, J. M., and Saven, J. G. (2000) Statistical theory of combinatorial libraries of folding proteins: Energetic discrimination of a target structure. *J. Mol. Biol. 296*, 281–294.
44. Fu, X., Kono, H., and Saven, J. G. (2003) Probabilistic approach to the design of symmetric protein quaternary structures. *Protein Eng. 16*, 971–977.
45. Douglas, T., Strable, E., Willits, D., Abdelaziz, A., Libera, M., and Young, M. (2002) Protein engineering of a viral cage for constrained nanomaterials synthesis. *Adv. Mater. 14*, 415–418.
46. Ochoa, W. F., Chatterji, A., Lin, T., and Johnson, J. E. (2006) Generation and structural analysis of reactive empty particles derived from an icosahedral virus. *Chem. Biol. 13*, 771–778.
47. Lee, S.-Y., Royston, E., Culver, J. M., and Harris, M. T. (2005) Improved metal cluster deposition on a genetically engineered tobacco mosaic virus template. *Nanotechnology 16*, S435−S441.
48. Hempstead, P. D., Yewdall, S. J., Fernie, A. R., Lawson, D. M., Artymiuk, P., Rice, D., Ford, G. C., and Harrison, P. M. (1997) Comparison of the three-dimensional structures of recombinant human H and horse L ferritins at high resolution. *J. Mol. Biol. 268*, 424–448.
49. Hubbard, S. J., and Thornton, J. M. (1993) NACCESS, Department of Biochemistry and Molecular Biology, University College of London.
50. Farigon, S., Arosio, P., Fracanzani, A. L., Cislaghi, V., Levi, S., Cozzi, A., Piperno, A., and Fiorelli, G. (1988) Characteristics and expression of binding sites specific for ferritin H-chain on human cell lines. *Blood 71*, 753–757.
51. Santambrogio, P., Cozzi, A., Levi, S., Rovida, E., Magni, F., Albertini, A., and Arosio, P. (2000) Functional and immunological analysis of recombinant mouse H- and L-ferritins from *Escherichia coli*. *Protein Expression Purif. 19*, 212–218.
52. Levi, S., Luzzago, A., Cesareni, G., Cozzi, A., Franceschinelli, F., Albertini, A., and Arosio, P. (1988) Mechanism of ferritin iron uptake: Activity of the H-chain and deletion mapping of the ferro-oxidase site. *J. Biol. Chem. 263*, 18086–18092.
53. Tamilarasan, R., and McMillin, D. R. (1986) Absorption spectra of d^{10} metal ion derivatives of plastocyanin. *Inorg. Chem. 25*, 2037–2040.
54. Ha, Y., Shi, D., Small, G. W., Theil, E. C., and Allewell, N. M. (1999) Crystal structure of bullfrog M ferritin at 2.8 Å resolution: analysis of subunit interactions and the binuclear metal center. *J. Biol. Inorg. Chem. 4*, 243–256.
55. Otwinowski, Z., and Minor, W., Eds. (1997) *Processing of X-ray Diffraction Data Collected in Oscillation Mode*, Vol. 276, Academic Press, New York.
56. McCoy, A. J., Grosse-Kunstleve, R. W., Storni, L. C., and Read, R. J. (2005) Likelihood-enhanced fast translation functions. *Acta Crystallogr. D 61*, 458–464.
57. Storoni, L. C., McCoy, A. J., and Read, R. J. (2004) Likelihood-enhanced fast rotation functions. *Acta. Crystallogr. D 60*, 432–438.
58. Jones, T. A., Zou, J.-Y., Cowan, S. W., and Kjeldgaard, M. (1991) Improved methods for building protein models in electron density maps and the location of errors in these models. *Acta Crystallogr. A 47*, 110–119.
59. Brünger, A. T., Adams, P. D., Clore, G. M., DeLano, W. L., Gros, P., Grosse-Kunstleve, R. W., Jiang, J. S., Kuszewski, J., Nilges, M., Pannu, N. S., Read, R. J., Rice, L. M., Simonson, T., and Warren, G. L. (1998) Crystallography & NMR system: A new software suite for macromolecular structure determination. *Acta Crystallogr. D 54*, 905–921.
60. Afonine, P. V., Grosse-Kunstleve, R. W., and Adams, P. D. (2005) The Phenix refinement framework. *CCP4 Newsl. 42*.
61. Welch, K. D., Reilly, C. A., and Aust, S. D. (2002) The role of cysteine residues in the oxidation of ferritin. *Free Radical Biol. Med. 33*, 399–408.
62. Petsev, D. N., Thomas, B. R., Yau, S.-T., and Vekilov, P. G. (2000) Interactions and aggregation of apoferritin molecules in solution: effects of added electrolytes. *Biophys. J. 78*, 2060–2069.
63. Granier, T., Gallios, B., Dautant, A., d'Estaintot, B. L., and Précigoux, G. (1997) Comparison of the structures of the cubic and tetragonal forms of horse-spleen apoferritin. *Acta Crystallogr. D 53*, 580–587.
64. Lawson, D. M., Artymiuk, P. J., Yewdall, S. J., Smith, J. M. A., Livingstone, J. C., Treffry, A., Luzzago, A., Levi, S., Arosio, P., Cesareni, G., Thomas, C. D., Shaw, W. V., and Harrison, P. M. (1991) Solving the structure of human H ferritin by genetically engineering intermolecular crystal contacts. *Nature 349*, 541–544.

BI8016735